Supplementary Material for

Twinning mediated intralayer frustration governs structural degradation in layered Li-rich oxide cathode

Tingting Yang[1, 2, #], Maolin Yang[1, #], Zhongyuan Huang[1], Rui Wang[3], Tao Zeng[1], Peng-Han Lu[2], Wenhai Ji[4], Zenan Li[5], Jun Wang[5], Rafal E. Dunin-Borkowski[2], Lei Jin[2*], Yinguo Xiao[1*]

[1]School of Advanced Materials, Peking University, Shenzhen Graduate School, Shenzhen 518055, PR China

[2]Ernst Ruska-Centre for Microscopy and Spectroscopy with Electrons, Forschungszentrum Jülich GmbH, 52425 Jülich, Germany

[3]Department of Engineering, University of Cambridge, Cambridge CB30FS, UK

[4]Spallation Neutron Source Science Center, Dongguan 523803, PR China

[5]School of Innovation and Entrepreneurship, Southern University of Science and Technology, Shenzhen 518055, PR China

[#]These authors (T. Yang and M. Yang) contributed equally to this work.

[*]E-mail addresses: l.jin@fz-juelich.de (L. Jin); y.xiao@pku.edu.cn (Y. Xiao).

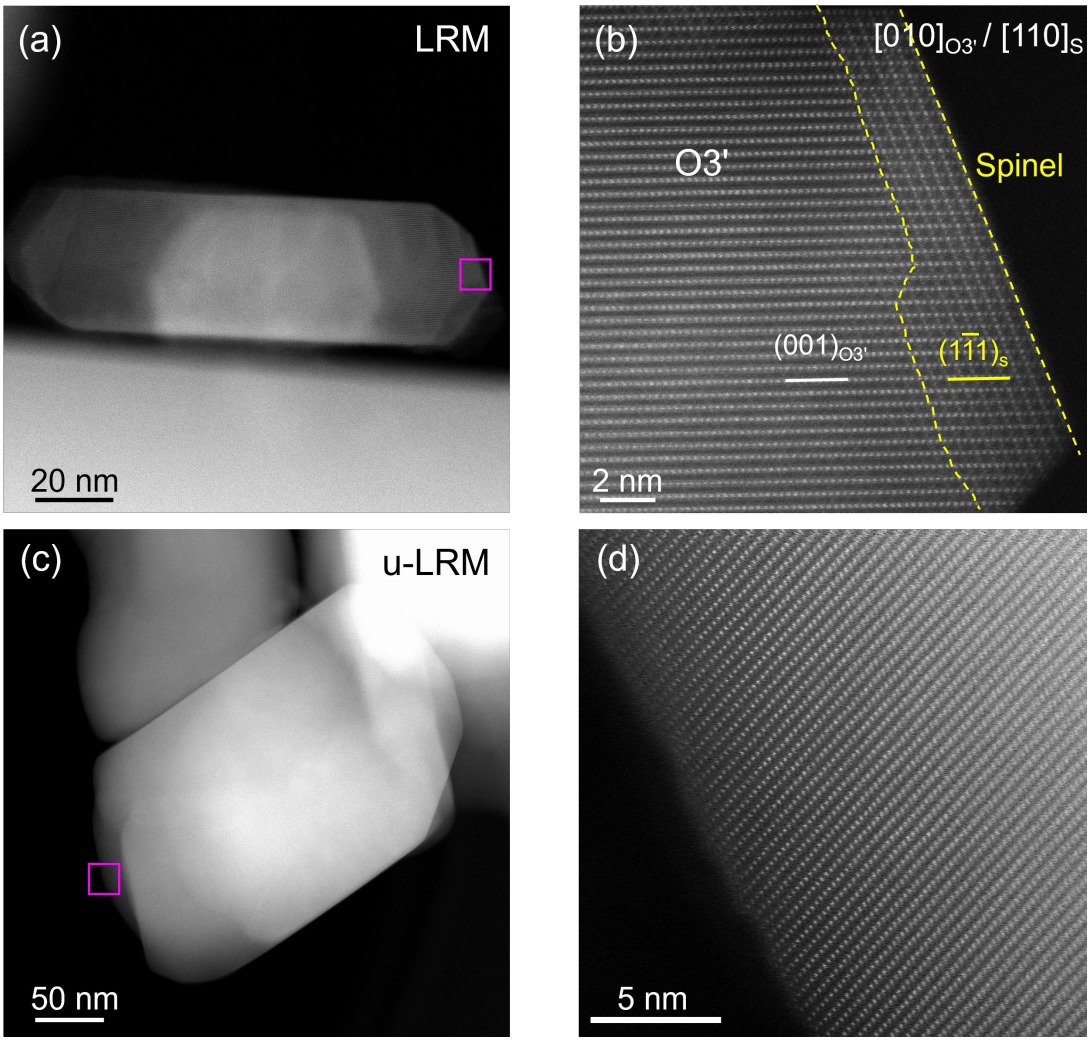

Supplementary Figure 1. (**a**) Low-magnification HAADF-STEM image of a pristine LRM nanoparticle. (**b**) Atomic-resolution HAADF-STEM image of the marked area in (**a**), showing a core/shell (O_3'/spinel) configuration. The orientation relationship between the spinel (S) shell and O_3' core is $[110]_S \parallel [010]_{O3'}$, $(1\bar{1}1)_S \parallel (001)_{O3'}$. (**c, d**) The morphology and the atomic-resolution HAADF-STEM image of the untreated LRM (u-LRM) nanoparticle.

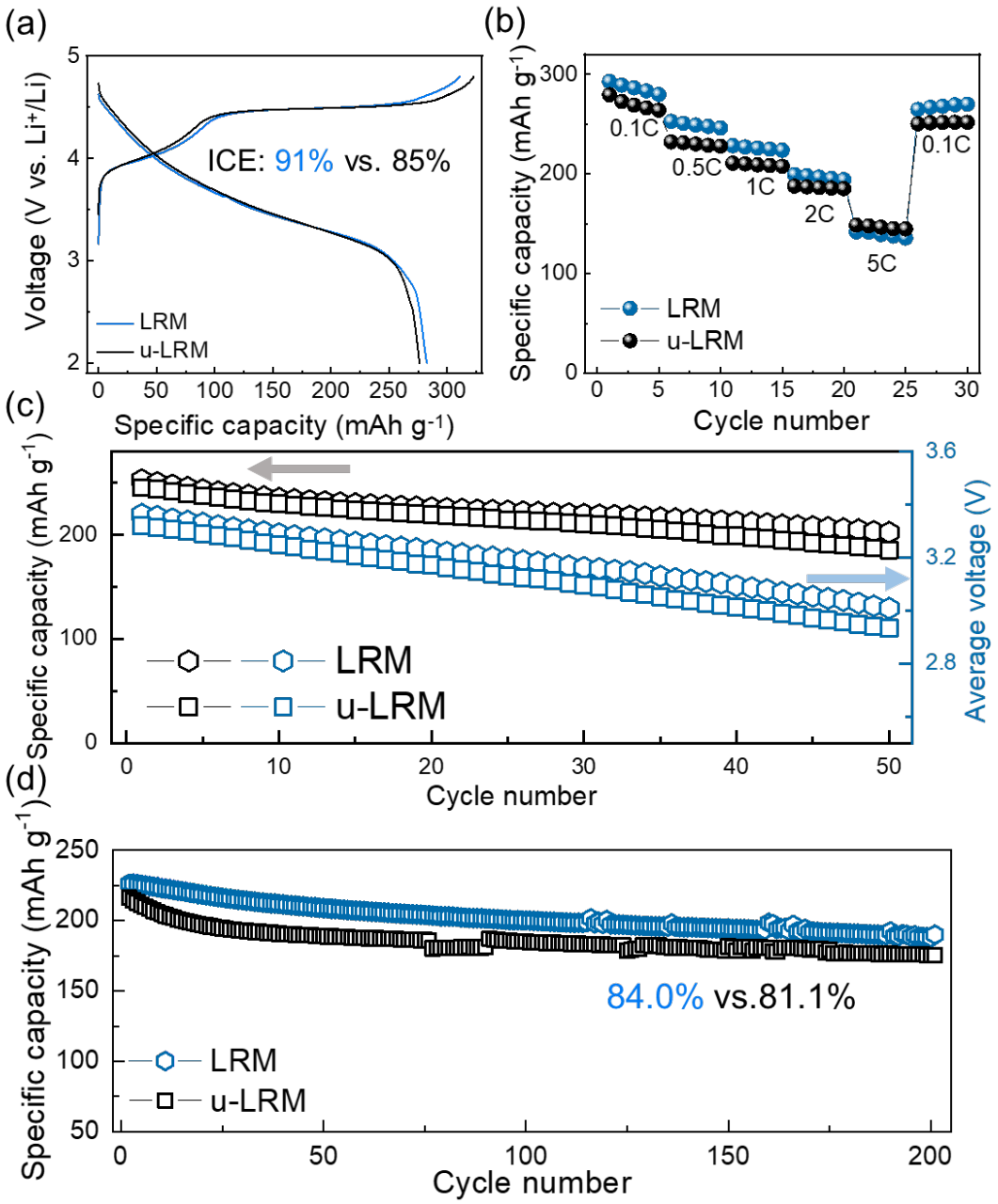

Supplementary Figure 2. Electrochemical LRM performance in a half cell. **(a)** Initial galvanostatic charge discharge (GCD) curve of the synthesized LRM and u-LRM during the first cycle within 2-4.8 V. **(b)** Rate performance of the synthesized LRM and u-LRM at various rates. **(c)** Long-term cycling retention and average voltage of the synthesized LRM and u-LRM at a rate of 0.5C (1C = 250 mA g^{-1}). **(d)** Long-term cycling retention of the synthesized LRM and u-LRM at a rate of 1C.

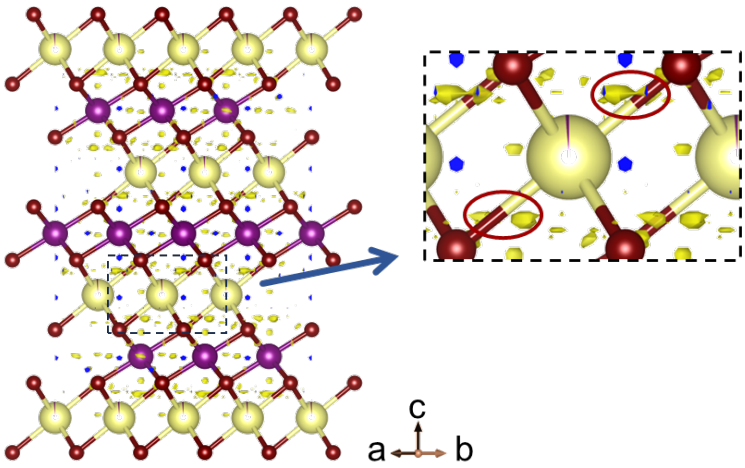

Supplementary Figure 3. Fourier difference map between observed data and O3' phase based on NPD result of LRM. Negative signal isosurface has been overlaid with a structural schematic of the O3 phase.

Rietveld refinement processes:

1. Calibration with Uncharged Neutron Diffraction:

A high-intensity neutron diffraction spectrum of the uncharged pouch cell was collected over an extended period of 60 minutes (compared to 30 minutes for each *operando* pattern). This allowed us to accurately determine the crystal structures of the electrochemically inactive Al and Cu current collectors. The structural parameters of these collectors were fixed, with only the 'scale' parameter adjusted to account for intensity variations due to differences in neutron beam flux.

2. Peak Shape Parameters:

Using the high-quality initial spectrum, peak shape factors for each compound involved in the *operando* processes were established and subsequently held constant during refinement.

3. Graphitic Anode Compounds:

The specific interplanar spacings of lithium-carbon compounds on the anode side (e.g., graphite, LiC_6, and LiC_{12}) remain unaffected by lithium intercalation or deintercalation. Therefore, lattice parameters for these phases were fixed based on the initial spectrum. Furthermore, the specific anode components could be clearly distinguished through diffraction peaks in the high d-value region.

4. Exclusion of Transition Metal Segregation in LRM Phases:

Based on STEM characterization results and to simplify the discussion, we did not consider elemental segregation of transition metals across the three LRM phases during refinement.

These adjustments led to a significantly improved goodness of fit across the full spectrum, thereby enhancing the reliability of the Rietveld refinement results and supporting a more accurate interpretation of the cathode's structural evolution.

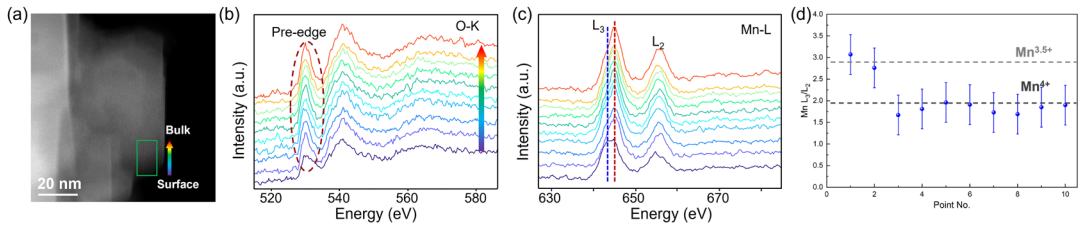

Supplementary Figure 4. (**a**) Annular dark-field STEM image of a pristine particle and (**b**, **c**) electron energy-loss spectra recorded at the (**b**) O-*K* and (**c**) Mn-$L_{2,3}$ edges from the marked area in (**a**). (**d**) Mn L_3/L_2 ratio calculated from (**c**). The dashed lines mark Mn valences of +3.5 and +4.0.[1]

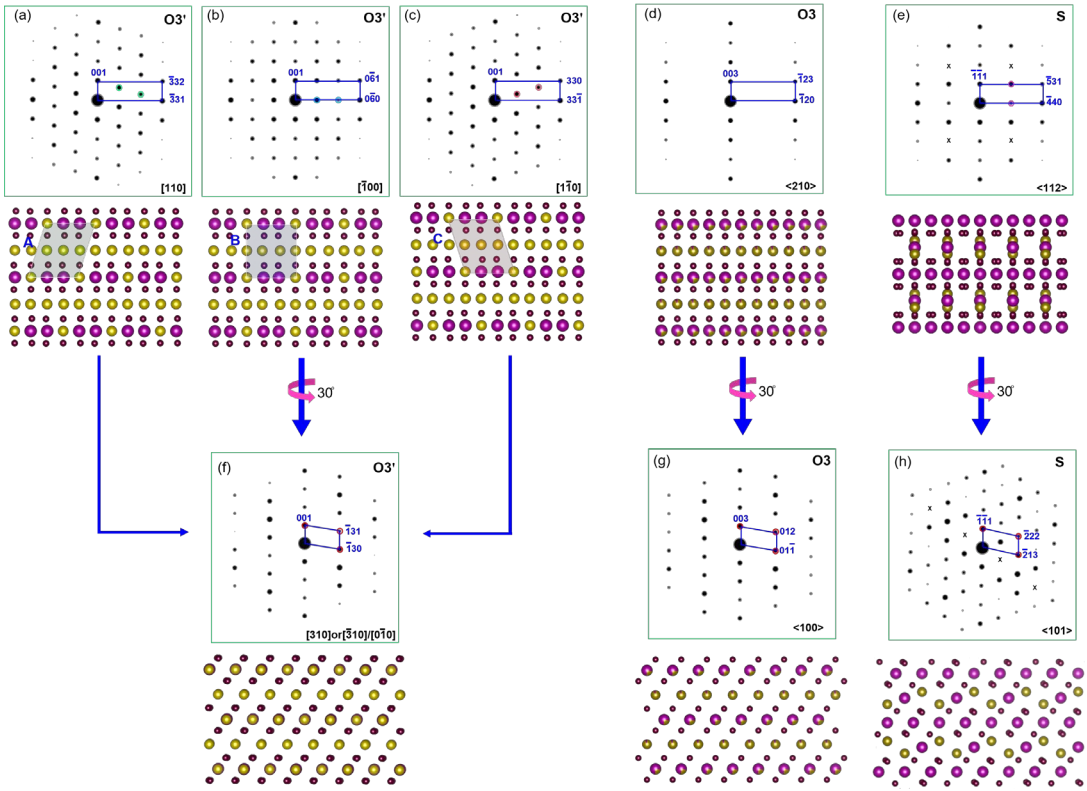

Supplementary Figure 5. Simulated diffraction patterns and corresponding atomic projections for O3', O3 and spinel (S), showing the orientation relationships among the three phases. (**a-c**) O3' [110], [$\bar{1}$00] and [1$\bar{1}$0] showing three configurations associated with TM-Li ordering. (**d**) O3 <210> projection showing TM-Li disordering. (**f**) O3 [310] (or [$\bar{3}$10]/ [0$\bar{1}$0]), along which all patterns are identical and TM-Li ordering becomes invisible. (**g**) O3 <100> showing the same patterns as (f). (**e**, **h**) Spinel <112> and <101> projections.

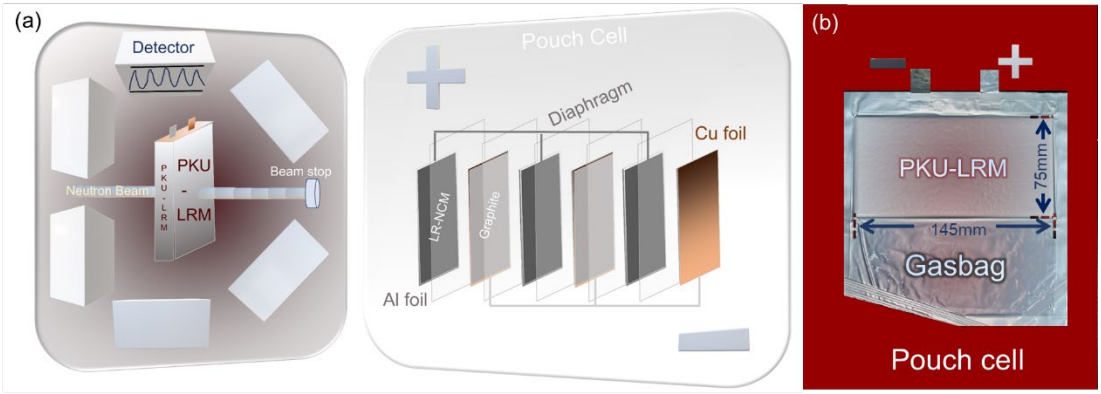

Supplementary Figure 6. (**a**) Schematic diagram of the *operando* neutron diffraction setup for the graphite || LRM pouch cell. (**b**) Photograph of an graphite || LRM pouch cell.

Graphite || LRM Pouch-cell	
Cathodes	**$Li_{1.2}Ni_{0.13}Co_{0.13}Mn_{0.54}O_2$**
Anode	**Graphite**
Pouch-cell Weight	**71.04 g**
Active Areas of Cathodes and Anodes (16 Poles of Each)	**145 × 75 mm^2 (Double-face)**
Cathode Mass Loading	**17.8 mg/cm^2**
Anode Mass Loading	**16.0 mg/cm^2**
N/P Radio	**1.1**
Electrolyte (1M LiF_6 TFTFE-FEMC-FEC)	**10 g**
Capacity of Cell (2.5 - 4.5 V)	**4 Ah**

Supplementary Figure 7. Design parameters of graphite || LRM pouch cell used in this work.

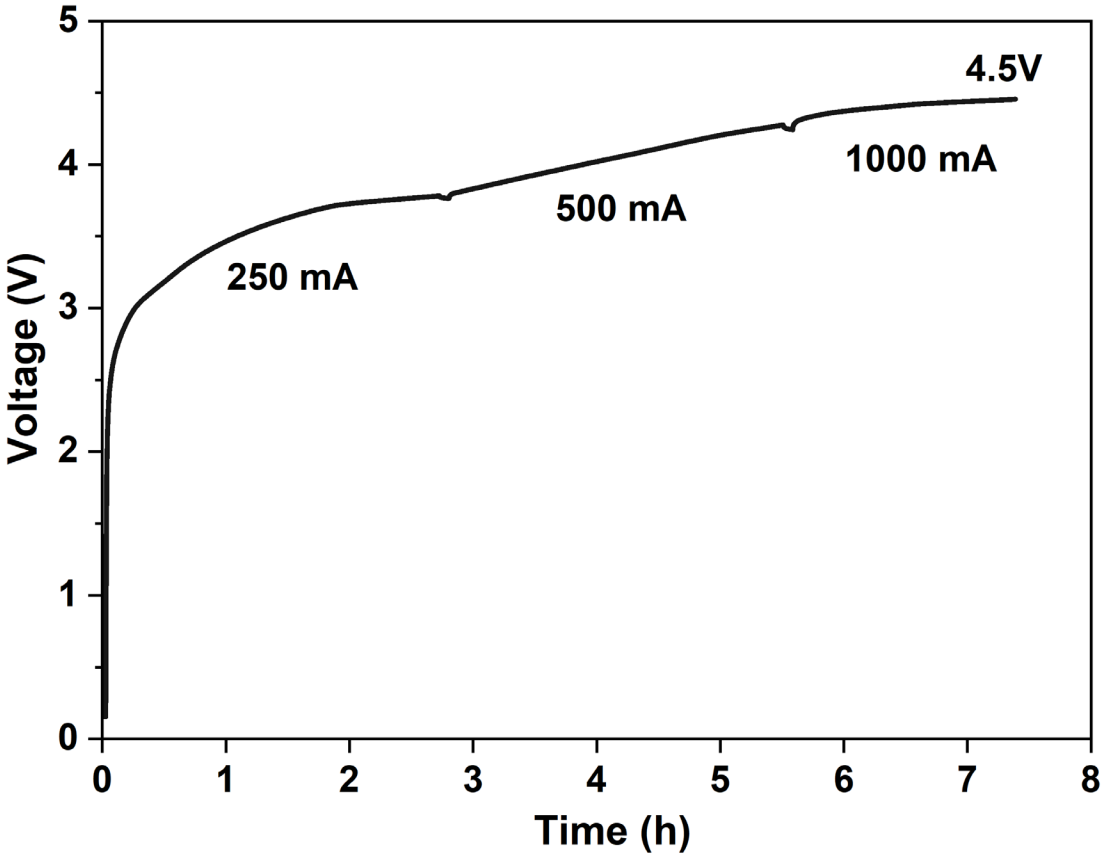

Supplementary Figure 8. The electrochemical curve of formation process in pouch cell.

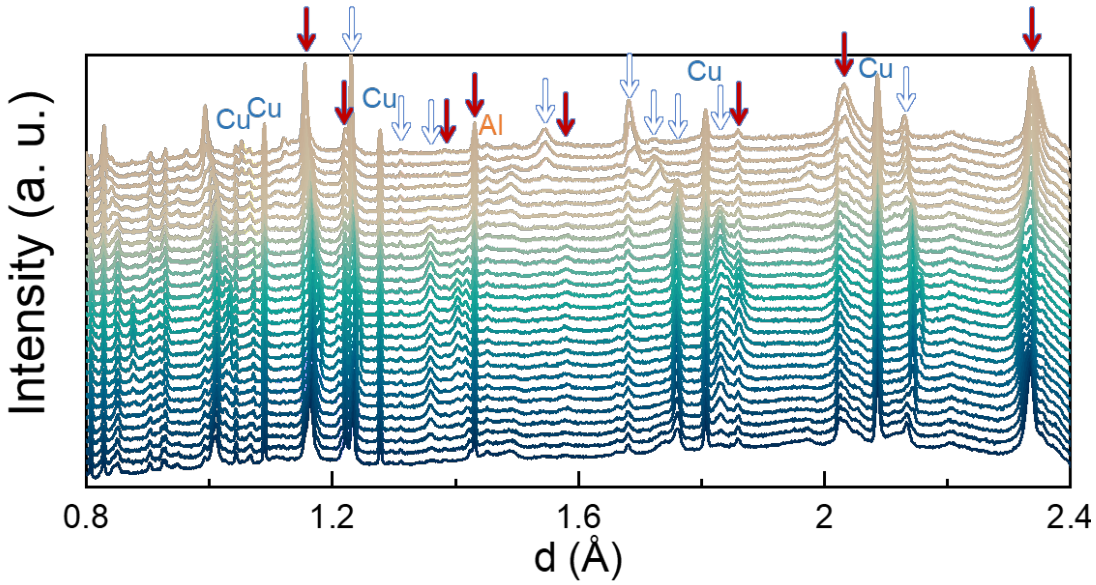

Supplementary Figure 9. The stacked plot of the operando neutron diffraction. The red arrow indexes the cathode, while the white arrow indexes the anode.

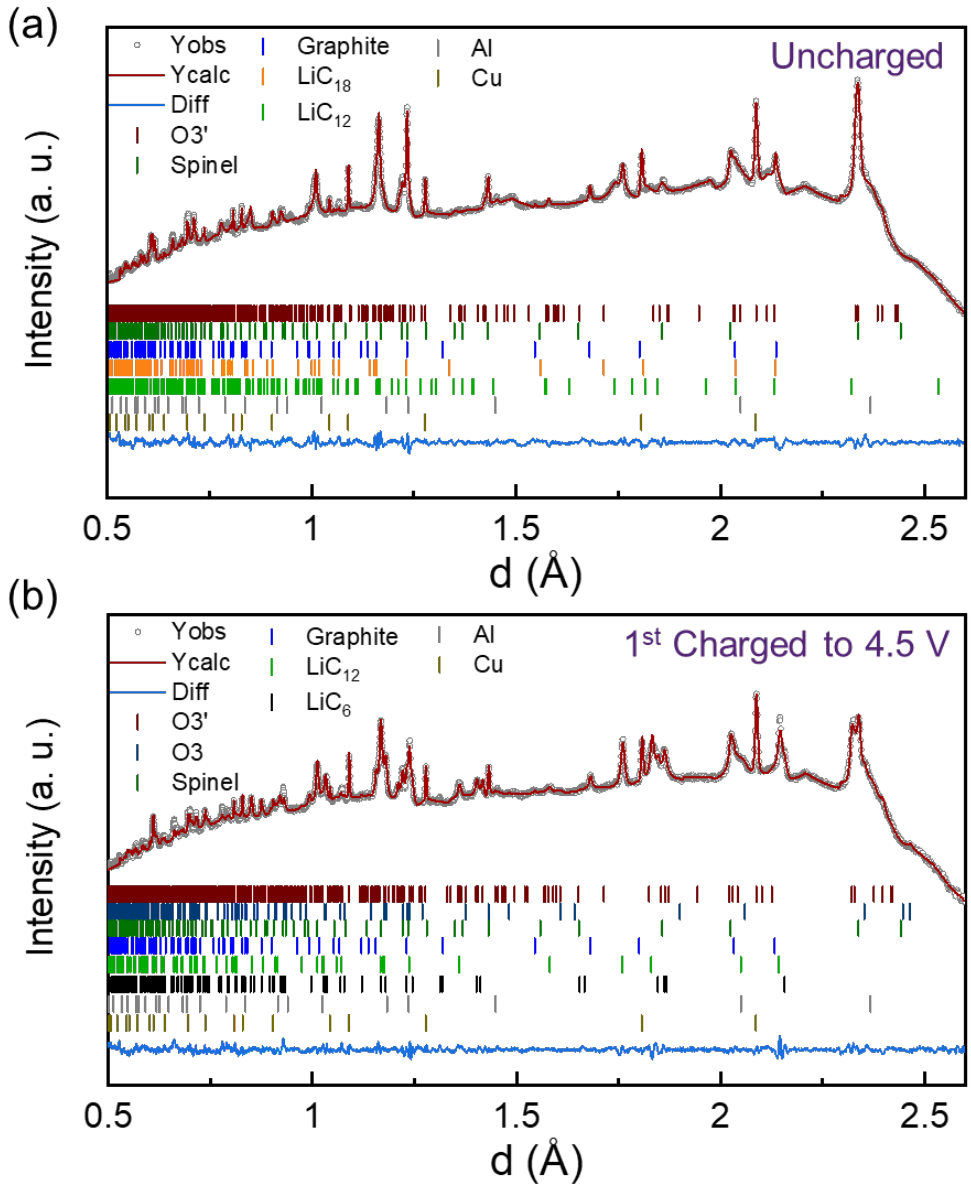

Supplementary Figure 10. (**a**, **b**) Refined neutron diffraction patterns recorded from the pouch cell (**a**) before and (**b**) after the first charge to 4.5 V. Bragg peak positions for the different phases, *i.e.*, different components in the pouch cell, are marked by short vertical bars in (**a**) and (**b**).

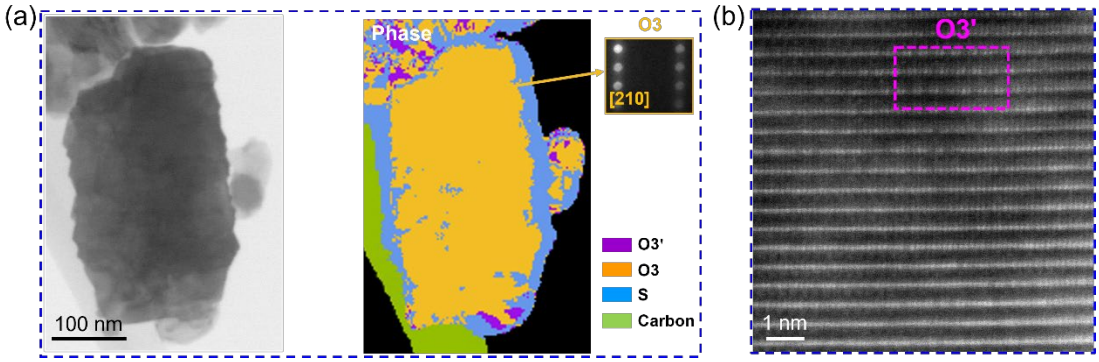

Supplementary Figure 11. Phase distribution in the cathode after first fully charged condition. (**a**) Phase mapping of the cathode after first fully charged along O3 [210] zone axis. (**b**) High-resolution HAADF-STEM image of the cathode after first fully charged, showing that only a small fraction of the O3' phase has remained, in agreement with the neutron diffraction results.

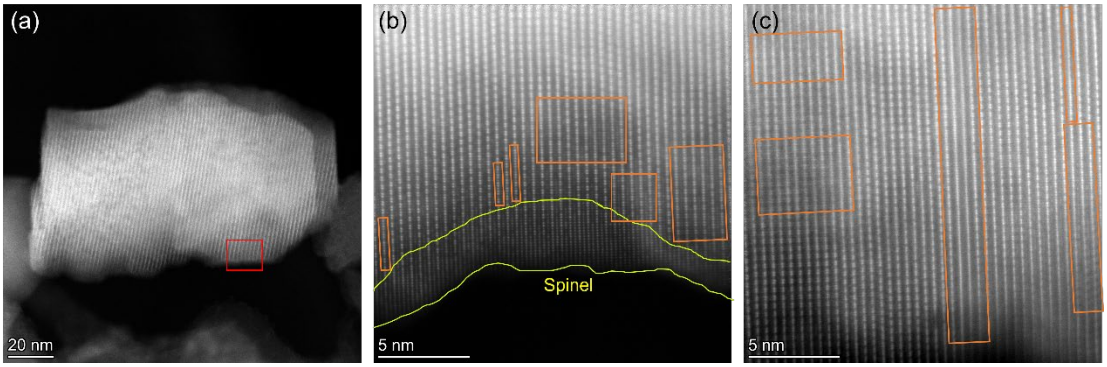

Supplementary Figure 12. (**a**) HAADF-STEM image showing an overview of a representative particle after first discharged to 2.5 V condition. (**b, c**) Atomic-resolution image of the area marked in (**a**), the O3 domains and the spinel phase are indicated by orange and yellow, respectively.

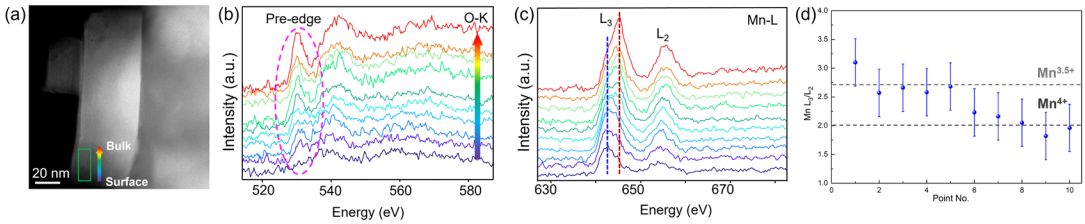

Supplementary Figure 13. (**a**) Annular dark-field STEM image and (**b**) O-*K* and (**c**) Mn-$L_{2,3}$ EELS fine structures recorded from the surface to the interior of a fully-charged LRM particle. (**d**) Mn L_3/L_2 ratio determined from (**c**), showing that the Mn valence does not change significantly after the first full charge.

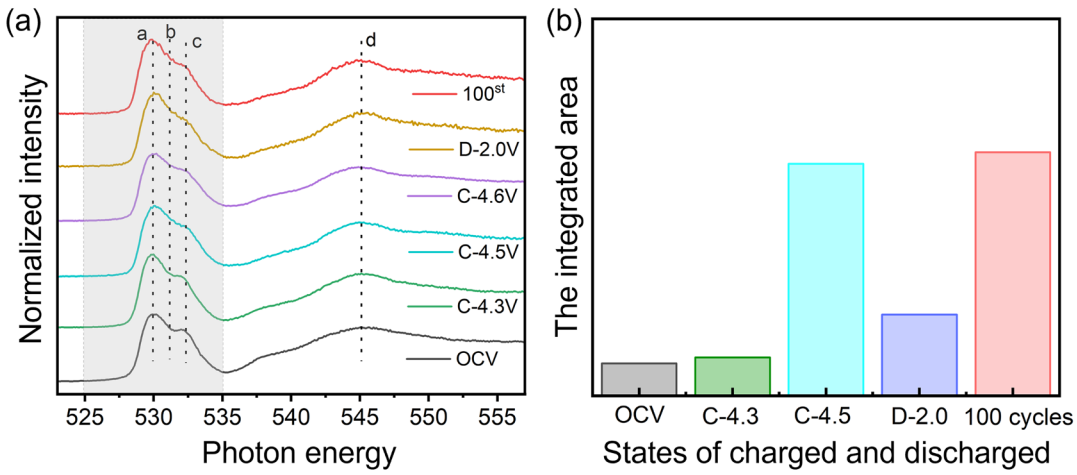

Supplementary Figure 14. (**a**) Normalized LRM O *K*-edge soft X-ray absorption spectra (sXAS) and (**b**) Integrated intensity between 525 and 535 eV for different charge/discharge states in the first cycle and after 100 cycles recorded in fluorescence yield mode.

Peaks a and c reflect O *2p*-Mn *3d* t_{2g} and O *2p*-Mn *3d* e_g orbital hybridization, respectively. Peak b emerged at high voltage (C-4.5 V), indicating O oxidation. The broadened peak d originates from the hybrid O *2p*-Mn *4sp* state. The integrated intensities from 525 to 535 eV reflect variations in O vacancies (holes). From OCV to C-4.3 V, the integrated intensities increase due to oxidation of TM atoms, which results in more empty orbitals. More O vacancies are generated on charging to 4.5 V. The integrated intensity decreases after discharging to 2.0 V, but remains higher than for OCV, implying O irreversibility during battery cycling. After 100 cycles (under OCV), the integrated intensity increases significantly, suggesting the formation of a large number of O vacancies and empty TM orbitals. This behavior is linked to the formation of a surface spinel structure.

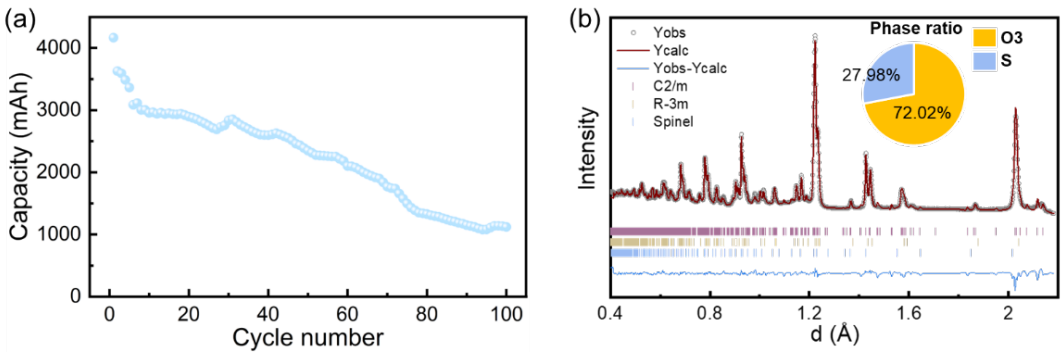

Supplementary Figure 15. (**a**) Long-term cycling retention of the pouch cell at a current of 4 A and at 2.0 – 4.5 V. (**b**) NPD and Rietveld refinement analysis of the LRM after 100 cycles. The inset sector plot shows the phase fraction distribution.

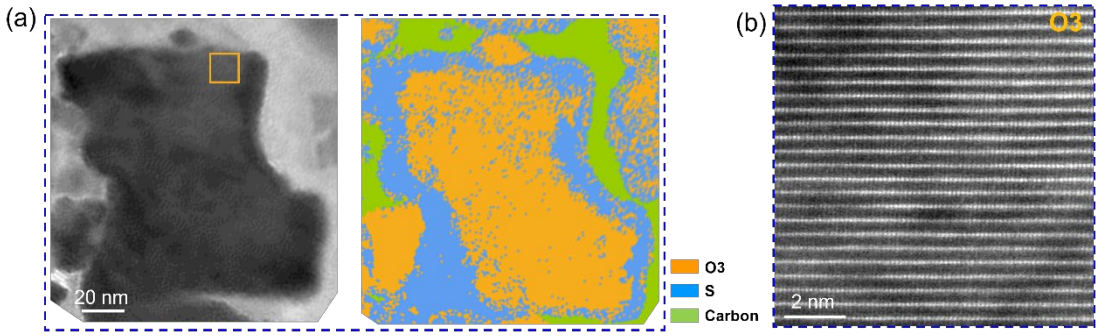

Supplementary Figure 16. (**a**) Phase mapping of the cathode after 100 cycles along O3 <210> zone axis. (**b**) High-resolution HAADF-STEM image showing that the atomic arrangement is disordered and no O3' phase is left after 100 cycles.

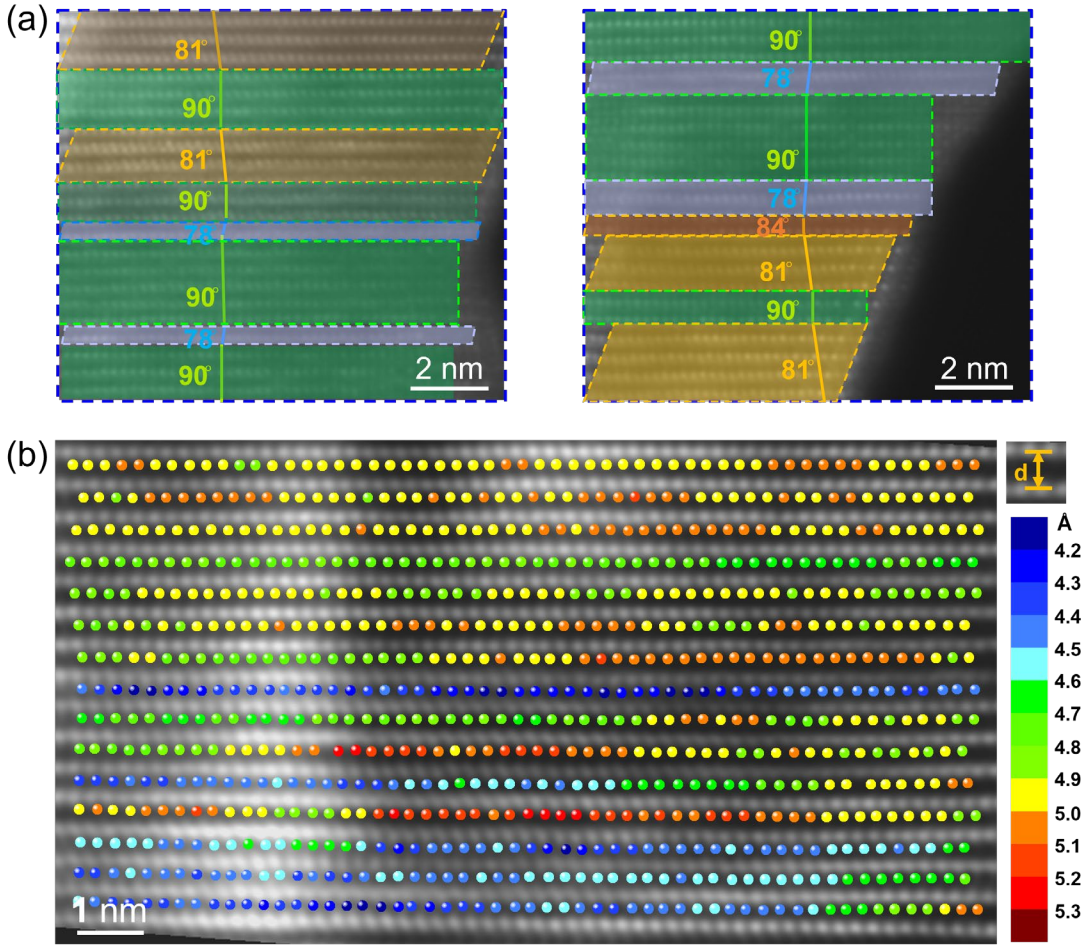

Supplementary Figure 17. (**a**) Atomic-resolution HAADF-STEM image of a cathode LRM particle charged to 4.5 V. (**b**) Simulated lattice value map of the area in Fig. 3d.

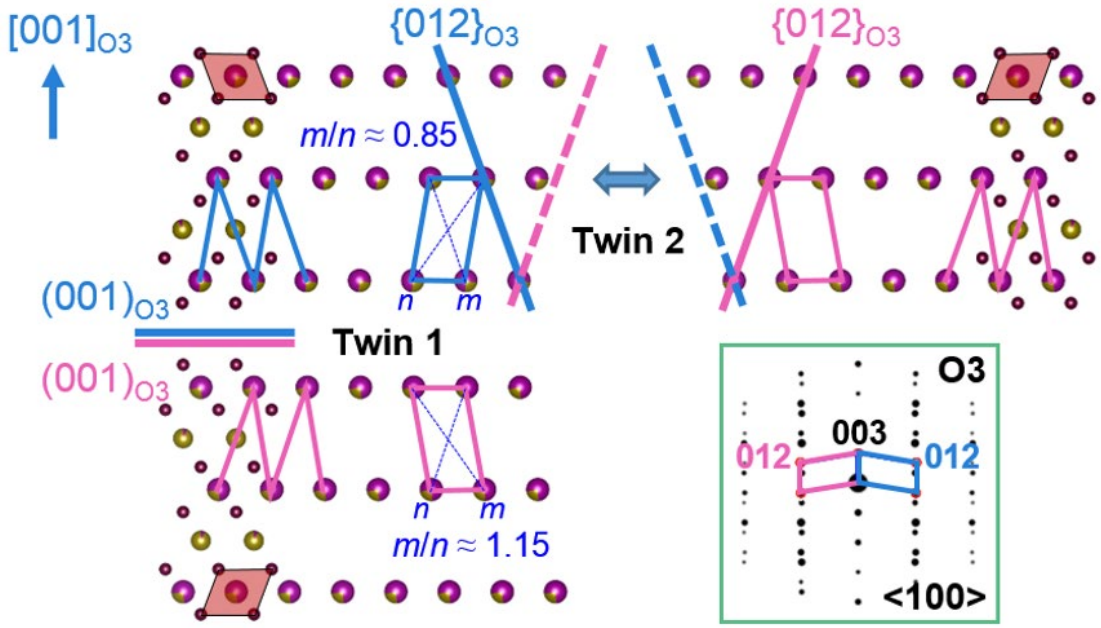

Supplementary Figure 18. Schematic illustration of two types of twinning configurations. Twin 1: $[001]_{O3}$ twin axis with twinning plane of $(001)_{O3}$, and Twin 2: $[001]_{O3}$ twin with twinning habit plane of $\{012\}_{O3}$. The simulated electron diffraction is calculated based on kinematical electron diffraction theory.

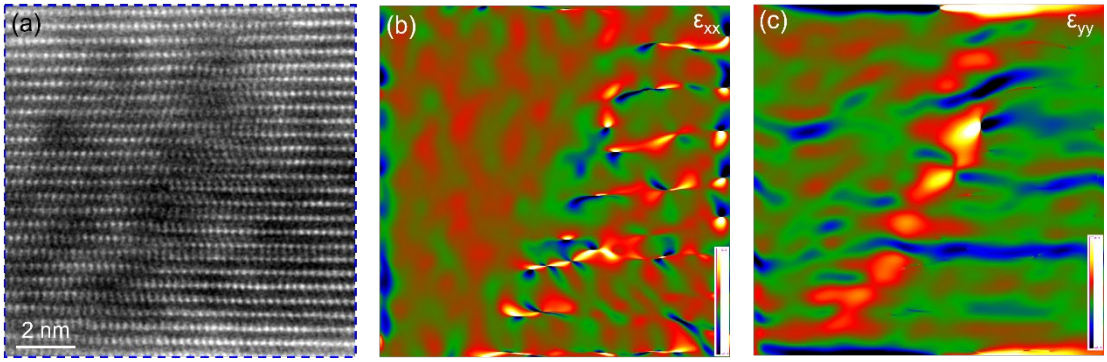

Supplementary Figure 19. (**b**) Horizontal ε_{xx} and (**c**) vertical ε_{yy} strain distributions obtained by applying geometrical phase analysis to the HAADF-STEM image shown in (**a**). The color scale spans strains of -20% (blue) to +20% (red).

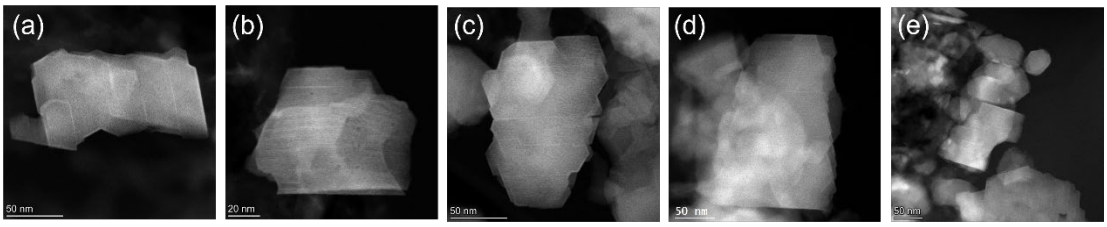

Supplementary Figure 20. Defects in the cathode material after 100 cycles.

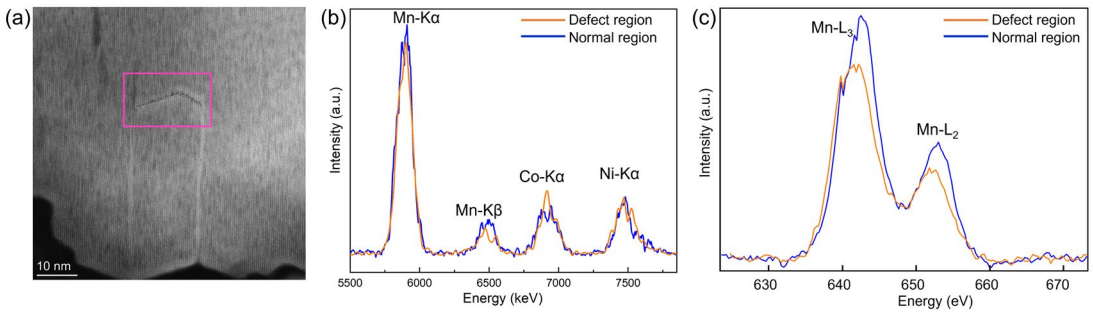

Supplementary Figure 21. (**a**) The overview HAADF-STEM image of LRM cathode after 100 cycles. (**b**) The EDS spectra showing the Mn, Co and Ni K edges from the specified region in (**a**). Decreased Mn concentration can be observed at the defect area. (**c**) The EELS spectra showing the Mn L edges of the selected area in (**a**), indicating the valence change of Mn in defect region.

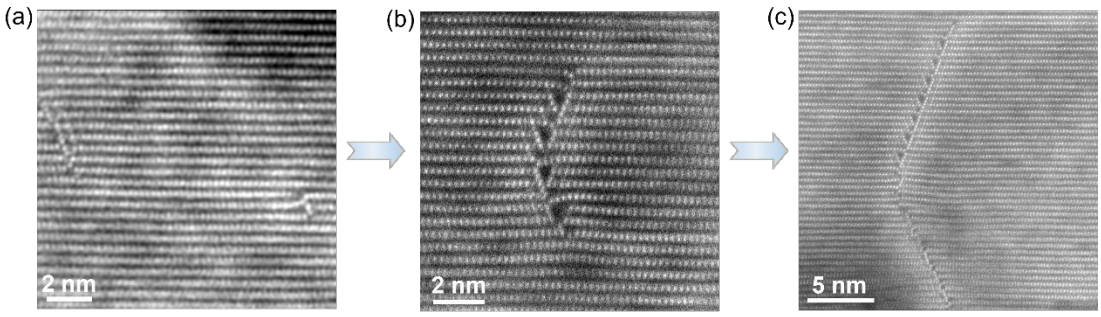

Supplementary Figure 22. Images showing the defect formation process.

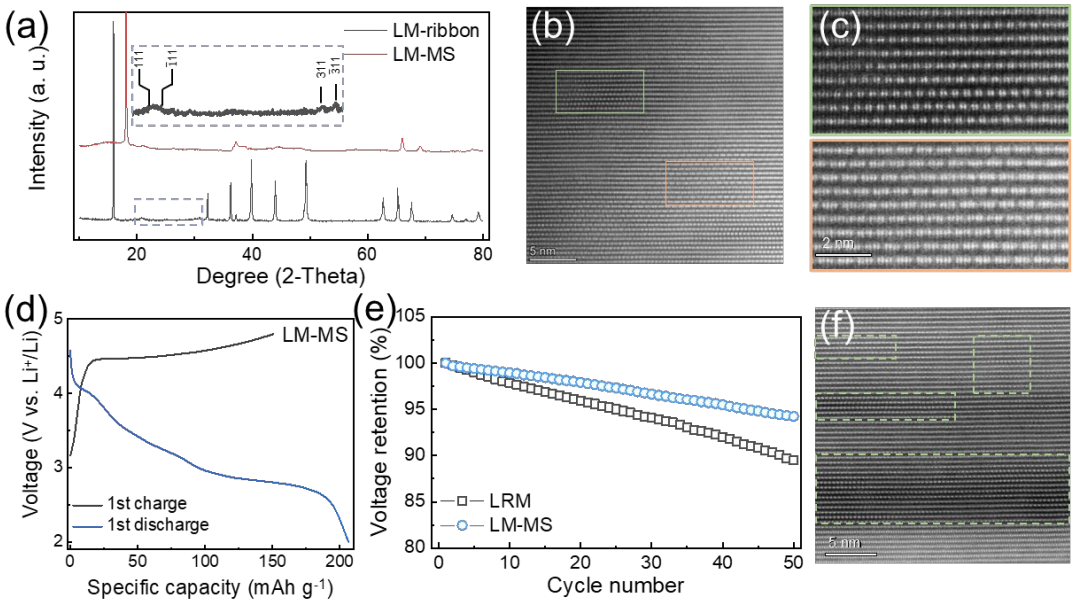

Supplementary Figure 23. (**a**) XRD patterns of $Na_{0.6}Li_{0.2}Mn_{0.8}O_2$ with a ribbon-type Li-Mn superlattice (denoted as LM-ribbon) and the ion-exchanged sample obtained via the molten salt method (denoted as LM-MS). (**b**) Low-magnification HAADF-STEM image of LM-MS. (**c**) High-resolution HAADF-STEM image of the marked region in (**b**), illustrating the atomic arrangement in the pristine LM-MS cathode, which features both honeycomb-type and ribbon-type structural domains. (**d**) Initial GCD curve of the synthesized LM-MS during the first cycle in the voltage range of 2–4.8 V. (**e**) Long-term average voltage retention of the synthesized LRM and LM-MS at a rate of 0.5C (1C = 250 mA g^{-1}). (**f**) HAADF-STEM image of LM-MS after 60 cycles at 0.5C.

Initially, a $Na_{0.6}Li_{0.2}Mn_{0.8}O_2$ cathode with a ribbon-type Li-Mn superlattice (denoted as LM-ribbon) was synthesized. Subsequently, a Li-rich oxide cathode with a partially preserved ribbon-type Li-Mn superlattice (denoted as LM-MS) was obtained via a molten salt substitution method, as shown in Supplementary Fig. 22b, c. This ribbon-type structure alleviated the intralayer rearrangement of transition metals, significantly reducing voltage hysteresis (Supplementary Fig. 22d). Furthermore, it mitigated interlayer migration of transition metals to some extent, effectively delaying voltage decay (Supplementary Fig. 22e).

Remarkably, after 60 cycles at 0.5C, the LM-MS cathode retained its transition metal layer superlattice without developing pore-like microstructures illustrated in Fig. 4e, f (Supplementary Fig. 19f). This indicates a substantial improvement in structural stability.

Supplementary Table 1. Proportions of O3' and spinel phase in the pristine cathode powder and crystal cell parameters.

O3' (*C2/m*): 97.27 at%						
Atom	***Wyckoff***	***x***	***y***	***z***	B_{iso} (Å^2)	***Occ.***
O	8*j*	0.251(3)	0.323(3)	0.224(1)	0.437(1)	0.997(2)
O	4*i*	0.219(1)	0	0.224(1)	0.437(1)	1
Mn	4*g*	0	0.169(2)	0	1.692(1)	0.783(2)
Li	4*g*	0	0.169(2)	0	1.692(1)	0.021(2)
Co	4*g*	0	0.169(2)	0	1.692(1)	0.194(1)
Ni	4*g*	0	0.169(2)	0	1.692(1)	0.001(1)
Li	2*b*	0	1/2	0	4.439(6)	0.561(5)
Ni	2*b*	0	1/2	0	4.439(6)	0.385(5)
Mn	2*b*	0	1/2	0	4.439(6)	0.053(1)
Co	2*b*	0	1/2	0	4.439(6)	0.001(1)
Li	4*h*	0	0.662(2)	1/2	1.011(2)	0.998(5)
Ni	4*h*	0	0.662(2)	1/2	1.011(2)	0.001(1)
Mn	4*h*	0	0.662(2)	1/2	1.011(2)	0.001(1)
Li	2*c*	0	0	1/2	1.389(4)	0.998(5)
Ni	2*c*	0	0	1/2	1.389(4)	0.001(1)
Mn	2*c*	0	0	1/2	1.389(4)	0.001(1)
a = 4.940(1) Å, b = 8.550(1) Å, c = 5.028(1) Å, $\alpha = \gamma$ =90°, β = 109.333(1)°.						
Spinel: 2.73 at%						
Atom	***Wyckoff***	***x***	***y***	***z***	B_{iso} (Å^2)	***Occ.***
O	32*e*	0.250(2)	0.250(2)	0.250(2)	1.871(7)	1
Mn	16*d*	1/2	1/2	1/2	0.569(8)	2/3
Co	16*d*	1/2	1/2	1/2	0.569(8)	1/6
Ni	16*d*	1/2	1/2	1/2	0.569(8)	1/6
Li	8*a*	1/8	1/8	1/8	0.868(5)	1
$a = b = c$ = 8.067(7) Å, $\alpha = \beta = \gamma$ = 90°.						
R_p: 2.19%, R_{wp}: 2.53%, R_{exp}: 0.14%.						

Supplementary Table 2. Proportions of O3' and spinel phase in the uncharged cathode and crystal cell parameters.

O3' (*C2/m*): 97.16 at%						
Atom	***Wyckoff***	***x***	***y***	***z***	***B_{iso} (Å^2)***	***Occ.***
O	8*j*	0.256(2)	0.324(5)	0.223(7)	0.252(1)	0.995(1)
O	4*i*	0.216(2)	0	0.223(7)	0.252(1)	1
Mn	4*g*	0	0.167(1)	0	2.059(2)	0.784(2)
Li	4*g*	0	0.167(1)	0	2.059(2)	0.021(2)
Co	4*g*	0	0.167(1)	0	2.059(2)	0.194(1)
Ni	4*g*	0	0.167(1)	0	2.059(2)	0.001(1)
Li	2*b*	0	1/2	0	5.667(6)	0.561(2)
Ni	2*b*	0	1/2	0	5.667(6)	0.385(2)
Mn	2*b*	0	1/2	0	5.667(6)	0.053(2)
Co	2*b*	0	1/2	0	5.667(6)	0.001(1)
Li	4*h*	0	0.662(3)	1/2	0.786(5)	0.956(4)
Ni	4*h*	0	0.662(3)	1/2	0.786(5)	0.001(1)
Mn	4*h*	0	0.662(3)	1/2	0.786(5)	0.001(1)
Li	2*c*	0	0	1/2	0.956(4)	0.956(4)
Ni	2*c*	0	0	1/2	0.956(4))	0.001(1)
Mn	2*c*	0	0	1/2	0.956(4)	0.001(1)
a = 4.947(3) Å, b = 8.544(1) Å, c = 5.029(8) Å, $\alpha = \gamma$ =90°, β = 109.25(3)°.						
Spinel: 2.84 at%						
Atom	***Wyckoff***	***x***	***y***	***z***	***B_{iso} (Å^2)***	***Occ.***
O	32*e*	0.246(3)	0.246(3)	0.246(3)	0.831(2)	1
Mn	16*d*	1/2	1/2	1/2	1.121(3)	2/3
Co	16*d*	1/2	1/2	1/2	1.121(3)	1/6
Ni	16*d*	1/2	1/2	1/2	1.121(3)	1/6
Li	8*a*	1/8	1/8	1/8	0.175(1)	1
$a = b = c$ = 8.091(2) Å, $\alpha = \beta = \gamma$ = 90°.						
R_p: 0.884%, R_{wp}: 1.09%, R_{exp}: 0.36%.						

Supplementary Table 3. Proportions and structural information about O3 and spinel phases in the LRM cathode after 100 cycles.

O3 (*R-3m*): 72.02 at%						
Atom	***Wyckoff***	***x***	***y***	***z***	B_{iso} **(Å²)**	***Occ.***
O	6*c*	0	0	0.736(5)	1.467(3)	0.997(9)
Li	3*a*	0	0	0	3.603(7)	0.431(3)
Ni	3*a*	0	0	0	3.603(7)	0.002(3)
Ni	3*b*	0	0	1/2	3.603(7)	0.127(3)
Li	3*b*	0	0	1/2	3.600(9)	0.082(3)
Mn	3*b*	0	0	1/2	3.600(9)	0.539(1)
Co	3*b*	0	0	1/2	3.600(9)	0.130(1)
$a = b = 2.840(8)$ Å, $c = 14.539(2)$ Å, $\alpha = \beta = 90°$, $\gamma = 120°$.						
Spinel: 27.98 at%						
Atom	***Wyckoff***	***x***	***y***	***z***	B_{iso} **(Å²)**	***Occ.***
O	32*e*	0.233(8)	0.233(8)	0.233(8)	0.213(1)	0.978(6)
Mn	16*d*	1/2	1/2	1/2	0.220(2)	2/3
Co	16*d*	1/2	1/2	1/2	0.220(2)	1/6
Ni	16*d*	1/2	1/2	1/2	0.220(2)	1/6
Li	8*a*	1/8	1/8	1/8	0.579(2)	0.728(2)
$a = b = c = 8.173(5)$ Å, $\alpha = \beta = \gamma = 90°$.						
R_p: 1.32%, R_{wp}: 1.47%, R_{exp}: 0.27%.						

Supplementary Table 4. Measured defect densities of the samples after 100 cycles.

	Particle 1	**Particle 2**	**Particle 3**	**Particle 4**	**Particle 5**
Number of defects	6	5	4	4	6

Supplementary References

1 Tan, H., Verbeeck, J., Abakumov, A., can Tendeloo, G. Oxidation state and chemical shift investigation in transition metal oxides by EELS. *Ultramicroscopy* **116**, 24-33 (2012).